Downshift of the Ni d band center over Ni nanoparticles in situ confined within an amorphous silicon nitride matrix

Norifumi Asakuma, Shotaro Tada, Tomoyuki Tamura, Erika Kawaguchi, Sawao Honda, Toru Asaka, Assil Bouzid, Samuel Bernard, Yuji Iwamoto

Downshift of the Ni d band center over Ni nanoparticles *in situ* confined within an amorphous silicon nitride matrix.

Norifumi Asakuma[a], Shotaro Tada[a,b], Tomoyuki Tamura[c], Erika Kawaguchi[a], Sawao Honda[a], Toru Asaka[a], Assil Bouzid[d], Samuel Bernard[d], Yuji Iwamoto[a*]

[a] Department of Life Science and Applied Chemistry, Graduate School of Engineering, Nagoya Institute of Technology, Nagoya, Japan

[b] Department of Metallurgical and Materials Engineering, Indian Institute of Technology Madras, Chennai, India

[c] Department of Applied Physics, Graduate School of Engineering, Nagoya Institute of Technology, Nagoya, Japan

[d] IRCER, CNRS, Univ. Limoges, Limoges, France

KEYWORDS: Electronic metal-support interaction, amorphous silicon nitride, polymer-derived ceramics, nanocomposite, d band center

ABSTRACT: Herein, nanocomposites made of Ni nanoparticles *in situ* distributed in an amorphous silicon nitride (Ni/a-Si_3N_4) matrix in the one hand and within an amorphous silicon dioxide (Ni/a-SiO_2) matrix in the other hand have been synthesized from a same Ni-modified polysilazane. In both compounds, the Ni/Si atomic ratio (0.06-0.07), the average Ni nanocrystallite size (7.0-7.6 nm) and the micro/mesoporosity of the matrix have been rigorously fixed. Hydrogen (H_2)- temperature-programmed desorption (TPD) profile analysis revealed that the activation energy for H_2 desorption at about 100 –130 °C evaluated for the Ni/a-Si_3N_4 sample (47.4 kJ mol^{-1}) was lower than that for the Ni/a-SiO_2 sample (68.0 kJ mol^{-1}). Mechanistic study with the X-ray photoelectron spectroscopy (XPS) analysis and density functional theory (DFT) calculations revealed that, at the Ni nanoparticles/matrix heterointerfaces, Ni becomes more covalently bonded to N atoms in the a-Si_3N_4 matrix compared to O atoms in the a-SiO_2 matrix. Therefore, by relying on experimental and theoretical studies, we have elucidated that the nickel-nitrogen (Ni-N) interactions at heterointerface lead to remarkable Ni d band broadening and downshifting of the d band center relative to those generated by the Ni-oxygen (Ni-O) interactions at heterointerface. This leads to the facilitated H_2 desorption experimentally observed in the Ni/a-Si_3N_4 sample.

INTRODUCTION

Energy-related environmental issues have grown as one of the greatest concerns throughout the world. For driving sustainable growth in our economic society, materials discovery, especially through the design of efficient catalysts, appears to be a key element in the energy transition.[1-3]

Many studies on transition metal (TM)-based catalysis have been conducted in catalytic reactions because their outermost shell d-electrons play a central role not only in the chemisorption of adsorbates, i.e., small gas molecules, but also in subsequent chemical reactions and transformations.[4,5] The d band theory well represents the relationship between the chemisorption and catalytic activity of TM.[6-9] Based on this theory, the d band center relative to the Fermi energy ($\varepsilon_d - E_F$), which is related to the density of states for d electrons of TM, is found to show a correlation with the binding strength between TM and adsorbates.[6-9] The down (up) shift of the d band center relative to the Fermi energy means that the less (higher) availability of empty antibonding states between the TM and adsorbate results in weaker (stronger) interactions between them.[8] On the one hand, the weak binding strength between TM and adsorbates results in the difficulty of the dissociative chemisorption of adsorbates, on the other hand, the strong binding strength results in the difficulty of the desorption of adsorbates during the catalytic reaction. As a result, there is an appropriate binding strength to maximize the catalytic activity.[6-9] Thus, many efforts have been paid for the optimization of the d band center of TM to enhance their catalytic performance.

Among them, the construction of electronic metal-support interaction (EMSI) is a promising strategy for modifying the electronic structure of active TM species, adjusting catalytic performance and tuning the adsorption behavior in a catalysis process.[10] Therefore, the choice of catalytic support is crucial for developing novel active catalysts. Silicon nitride (Si_3N_4) is an attractive material as a catalytic support because of its surface nitrogen atoms (e.g., amino groups) expected to electronically interact with the loaded TM.[11,12]

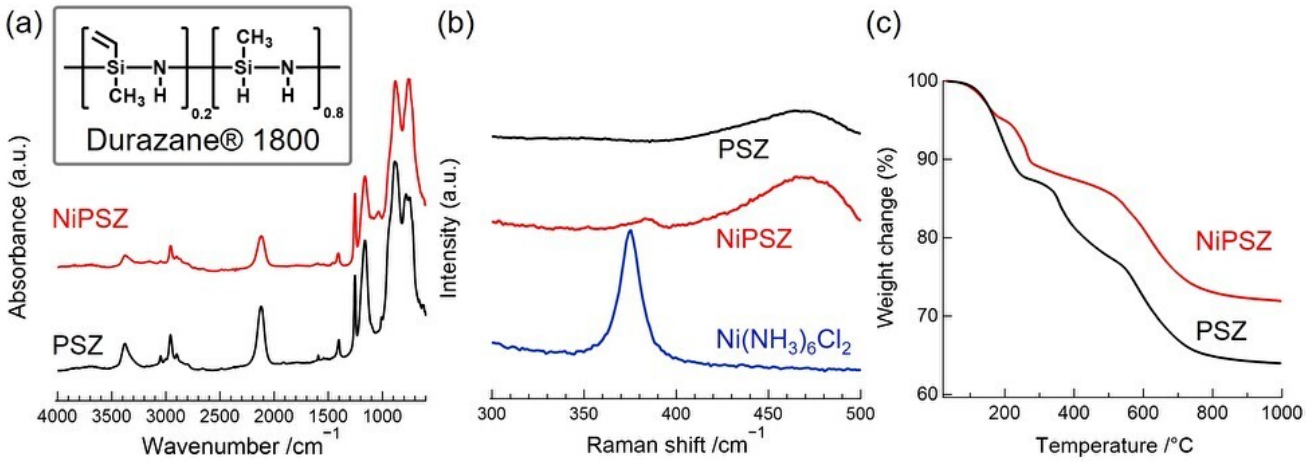

Figure 1. Chemical bonding natures and pyrolysis behavior of single source precursors: (a) ATR-FTIR spectra of as-received **PSZ** (black line) and **NiPSZ** (red line) samples with the inset of the chemical structure of Durazane®1800. (b) Raman spectra of as-received **PSZ** (black line), **NiPSZ** (red line), and $Ni(NH_3)_6Cl_2$ (blue line) samples. (c) TG-curves under flowing He of as-received **PSZ** (black line), **NiPSZ** (red line) samples.

However, Si_3N_4, regardless of amorphous or crystalline states, easily reacts with water, resulting in the formation of an oxidized surface layer.[13,14] This poor stability against hydrolysis makes difficult the application of conventional impregnation methods to deposit TM nanoparticles on Si_3N_4 underlining the importance of a novel synthetic route to TM/Si_3N_4 composite. To overcome this limitation, we recently reported the *in situ* formation of TM nanoparticles embedded within an amorphous Si_3N_4 (TM /a-Si_3N_4, TM = Co[15], Ni[16]) in anhydrous conditions through a precursor route called the Polymer-Derived Ceramics (PDC) route. Additionally, the surrounding matrix generally facilitates the EMSI because of the larger contact area between TM and the matrix.[17]

In this work, the electronic interaction between Ni nanoparticles and a-Si_3N_4 matrix is deeply investigated by both experimental and theoretical studies: a polymer-derived Ni/amorphous silicon carbonitride (a-SiCN) with a controlled and an average crystallite size of Ni of about 5 nm has been successfully converted into Ni nanoparticles embedded within H_2 gas permeable micro/mesoporous a-Si_3N_4 (Ni/a-Si_3N_4) and amorphous silicon dioxide (Ni/a-SiO_2) matrices having a Ni average particle sizes of 7.6 and 7.0 nm, respectively. The close average sizes of Ni nanoparticles (NPs) in Ni/a-Si_3N_4 and Ni/a-SiO_2 samples are crucial in an investigation of the effect of the a-Si_3N_4 matrix since the EMSI highly depends on the particle size of TM.[18,19] The hydrogen adsorption and desorption properties of both systems are compared by means of temperature-programmed desorption of hydrogen (H_2-TPD) to clarify the effect of EMSI. Additionally, the local electronic interaction around the Ni/matrix hetero interface is evaluated for the two different matrix systems by X-ray photoelectron spectroscopy (XPS) and discussed with a set of models theoretically predicted by the density functional theory (DFT) calculations.

Results and Discussion

We synthesized a Ni-modified polysilazane as a precursor for the *in situ* growth of Ni NPs in an amorphous Si-based matrix (The experimental procedure is described in supporting data). The commercially available poly(vinylmethyl-*co*-methyl)silazane (label hereafter **PSZ**) is used as the matrix precursor. Ni complex, hexaammine nickel(II) dichloride ($Ni(NH_3)_6Cl_2$) is applied as a Ni source. To investigate the chemical bonding states of the Ni-modified polysilazane (**NiPSZ**), ATR-FTIR spectroscopic analysis has been performed.

The as-received **PSZ** as a reference (black line in Figure 1 (a)) presents typical absorption bands of poly(vinylmethyl-co-methyl)silazane; 3379 (νN-H), 3048 (νC_{sp2}-H), 2957 (νC_{sp3}-H), 2899 (νC_{sp3}-H), 2120 (νSi-H), 1592 (νC=C), 1403 (δC_{sp2}-H, vinyl), 1254 (δSi-CH_3), 1161 (δN-H), 886 (νSi-N-Si), 782 cm^{-1}(Si-C),[20,21] respectively. **NiPSZ** shows similar absorption bands, however, it should be noted that compared with as-received **PSZ**, the absorption band intensity relative to the νSi-H (2120 cm^{-1}) and δC_{sp2}-H (vinyl group, 3050 cm^{-1}) decreases in **NiPSZ** as shown in Table S1 and Figure 1 (a) indicating the occurrence of reactions involving both units. As already reported by our group,[22] we suggest that hydrosilylation reactions between the Si-H and C=C occur and are probably catalytically promoted by Ni^{2+} species. Additionally, the relative intensity of the νN-H bond at 3379 cm^{-1} also decreases in **NiPSZ** although $Ni(NH_3)_6Cl_2$ as Ni precursor monomer has amine ligands. This means that dehydrogenation reactions between N-H and Si-H in polysilazane are also promoted and possibly catalyzed by the Ni^{2+} species, which has already been suggested in our previous works.[16,22] Therefore, the degree of cross-linking of **NiPSZ** is expected to increase compared to **PSZ** because of the formation of carbosilane chains (hydrosilylation) and -Si-N- bonds (dehydrogenation) in the **PSZ** network.

The Raman spectrum of $Ni(NH_3)_6Cl_2$ in Figure 1 (b) shows a typical peak centered at 375 cm^{-1} assigned to the Ni-N bond in $[Ni(NH_3)_6]^{2+}$.[23] This band in **NiPSZ** shifts to a higher wavenumber (387 cm^{-1}). It is reported that the Ni-N peak in $[Ni(NH_3)_2]^{2+}$ appears at a higher wavenumber, compared with that in $[Ni(NH_3)_6]^{2+}$.[23] Thus, this shift is clear evidence of the elimination of the NH_3 ligands from $Ni(NH_3)_6Cl_2$ to afford $Ni(NH_3)_2Cl_2$ or $NiCl_2$ during the synthesis of **NiPSZ**. Combined with the ATR-FTIR results, the Ni^{2+} species

coordinated by the polysilazane network could catalyze the hydrosilylation and dehydrogenation reactions of polysilazane networks, and the possible coordination structure of single source precursor is shown in Scheme 1.

Scheme 1. Dehydrogenation and hydrosilylation reactions in polysilazane catalyzed by Ni^{2+} species and possible coordination structure of single source precursor**.**

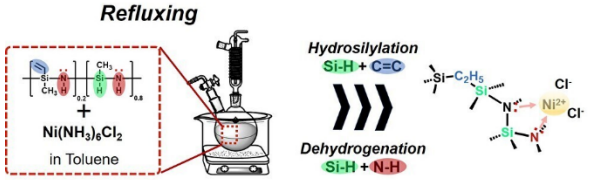

The chemical bonding state of a preceramic polymer affects its ceramic conversion process. Hence, the thermal behavior of **NiPSZ** and the reference **PSZ** have been monitored using TG-MS analysis under flowing inert gas (He). TG-curves in Figure 1 (c) show that major mass loss happens below 800 °C in both samples. However, compared with **PSZ**, the mass loss of **NiPSZ** is apparently reduced in the lower temperature range from 100 to 500 ºC. It is well reported that the residual reaction solvent and lower molecular weight oligomers are evolved in the temperature regime of the conversion of preceramic polymers.[16,24-26] Therefore, the observed decrease in the mass loss can be ascribed to the formation of a highly cross-linked polysilazane network achieved for the **NiPSZ** sample as indicated by the ATR-FTIR spectroscopic analysis. Simultaneous MS analysis (Figures S2 (a,b)) also supports the cross-linking occurrence of single source precursors. As shown in Figure S2, many fragment peaks derived from the polysilazane with lower molecular weight are detected in the case of **PSZ** whereas the dominant gaseous species detected for the **NiPSZ** are residual toluene (m/z = 91) used as the reaction solvent and ammonia (NH_3, m/z = 17) which is generally evolved during the transamination of polysilazane.[16,24]

Our previous work[16] reported the *in situ* formation of Ni nanoparticles embedded within amorphous silicon nitride through the pyrolysis of $NiCl_2$-modified perhydropolysilazane (PHPS) as a carbon-free precursor system. It was pointed out that the early *in situ* formation of nickel nitride species with the formation of chlorosilane species as by-products could trigger the nucleation and subsequent crystallization of nickel within the amorphous silicon nitride matrix. In this study, chlorosilane species (m/z = 93,95, Figure S3 (a)) are detected at 400–550 °C in **NiPSZ**; approximately 200 °C higher than the temperature range at which they occur in $NiCl_2$-modified PHPS. Thus, we further discuss the difference between the carbon-free Ni-modified PHPS and carbon containing—as methyl and vinyl substituent groups—**Ni PSZ** systems.

It is generally accepted that alkyl groups are electron-donating,[27] and thus silyl cation can be stabilized by the alkyl group bonded to the silicon. This consequently restricts the nucleophilic attack of the chlorine anion on the silicon cation center to afford the chlorosilane species formed in situ. Moreover, a considerable steric hindrance due to the methyl and vinyl group substitutions on the silicon atom could also restrict the nucleophilic attack. Therefore, the formation temperature of the byproduct chlorosilanes in the **NiPSZ** sample occurs at higher temperatures. In this study, the pyrolysis temperature for the synthesis of **Ni/a-SiCN** was set over the onset of the evolution temperature of monochlorosilane species, i.e., $T > 400$ °C.

The phase compositions of pyrolyzed and annealed samples have been investigated by the XRD analysis (Figure 2 (a)). The **Ni/a-SiCN** sample shows a broad peak derived from (111) lattice planes of fcc metal Ni nanocrystallites (JCPDS No. 04-002-7521, 2θ = 44.3 °). No peaks coming from the matrix appear in the XRD pattern as a consequence of the disordered structure of the ternary silicon carbonitride matrix. The average crystallite size for the Ni (111) plane based on the Scherrer equation was found to be 5.1 nm. XRD patterns for annealed samples (**Ni/a-Si_3N_4** and **Ni/a-SiO_2**) also show a broad peak derived from (111) lattice planes of fcc metal Ni nanocrystallites and the matrix supports in those systems are also X-ray amorphous. The XRD pattern of **NiO/a-SiO_2** sample in Figure S4 is composed of a broad peak at 2θ =15–30° and three more sharp peaks at 2θ =37.2, 43.3, and 63.1° which completely matches with the peak positions of amorphous SiO_2[28] and NiO (JCPDS No. 01-078-0423), respectively. Thus, one can claim that the **Ni/a-SiCN** sample was successfully converted into **Ni/a-SiO_2** system after annealing under air at 550 °C and subsequent H_2 reduction at 400 °C to restrict the oxidation of Ni nanoparticles. The average crystallite sizes for the Ni (111) plane of **Ni/a-Si_3N_4** and **Ni/a-SiO_2** are calculated to be 7.6 and 7.0 nm, respectively. These values can confirm that the aligning of particle size was successfully achieved to ideally measure the H_2 adsorption and desorption properties and to understand the effect of the catalytic support matrix on such properties.

To assess the local structure of the two compounds in detail, high resolution TEM (HRTEM) measurements have been performed. As shown in Figures 2 (b-g), highly dispersed dark dots are observed in all samples. The TEM images in Figures 2 (b,d,f) indicate the dark dots with a lattice spacing of 0.204 nm, corresponding to the d-spacing of the lattice plane of (111) direction of the fcc cubic Ni structure (JCPDS No. 04-002-7521) which is consistent with the phase identified in the X-ray diffractogram (Figure 2 (a)). In addition, the high-resolution TEM images in Figures 2 (c,e,g) confirm that Ni nanoparticles are surrounded by an amorphous matrix and this amorphous state is maintained even after the annealing treatment for the synthesis of **Ni/a-Si_3N_4** and **Ni/a-SiO_2**. The presence of this matrix offers thermal stability to the materials and prevents further sintering of Ni nanoparticles.[29] This nanocomposite-type structure is effective for the investigation of EMSI according to the fact that the contact area of the metal-support interface becomes larger.[17] The corresponding size distribution of Ni nanoparticles by counting 50 specimens, as displayed in Figures S5 (a-c), is relatively narrow in all samples: an average size of nanoparticles of 5.8, 8.1, and 7.8 nm is calculated for **Ni/a-SiCN**, **Ni/a-Si_3N_4**, and **Ni/a-SiO_2**, respectively.

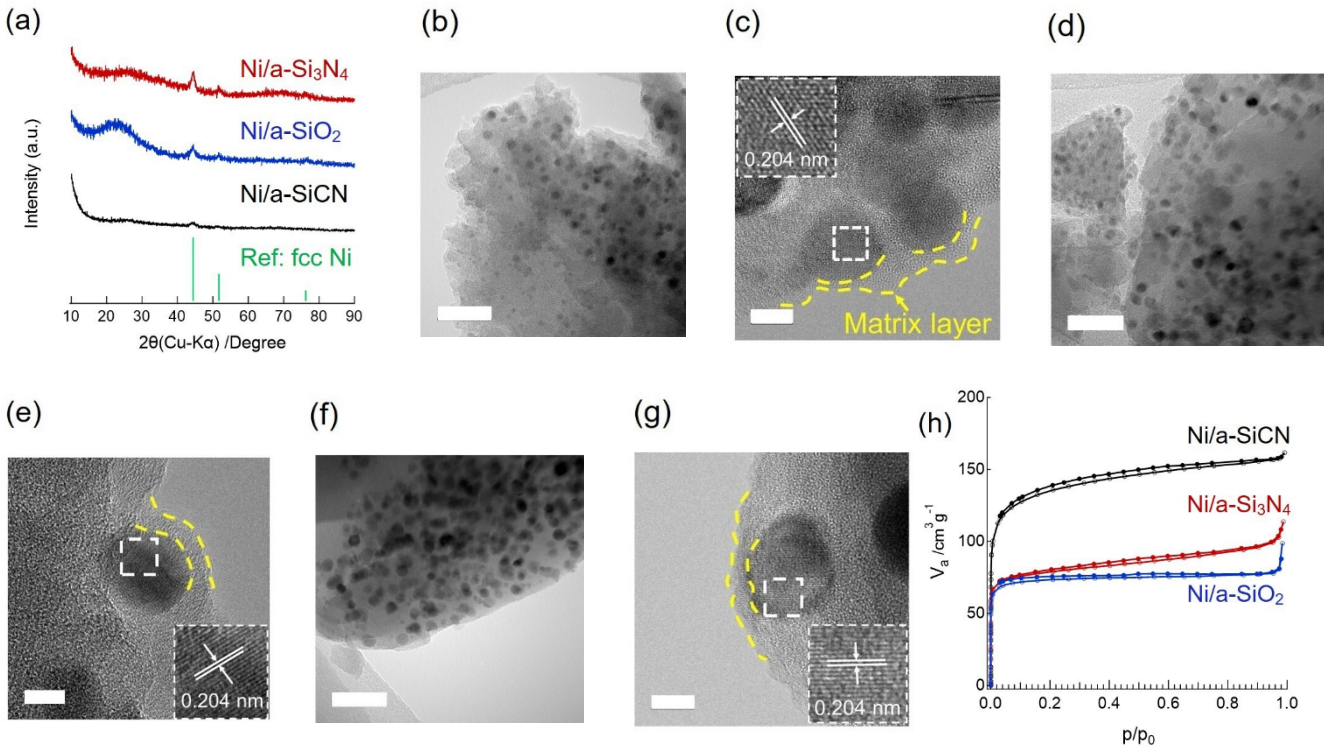

Figure 2. Properties of polymer-derived **Ni/a-SiCN**, **Ni/a-SiO₂**, and **Ni/a-Si₃N₄** samples: (a) Powder X-ray diffraction patterns of **Ni/a-SiCN** (black line), **Ni/a-SiO₂** (dark-blue line), and **Ni/a-Si₃N₄** (dark-red line). The vertical green lines represent the reference of fcc Ni (JCPDS No. 04-002-7521). TEM (Scale bar: 50 nm) and HRTEM (Scale bar: 5 nm) images of (b, c) **Ni/a-SiCN**, (d, e) **Ni/a-Si₃N₄**, and (f, g) **Ni/a-SiO₂** samples. (h) N_2 adsorption (open circle) and desorption (solid circle) isotherms at -196 °C for **Ni/a-SiCN** (black line), **Ni/a-Si₃N₄** (dark-red line), and **Ni/a-SiO₂** (dark-blue line) samples.

Table 1. Elemental composition of **Ni/a-SiCN**, **Ni/a-Si₃N₄**, and **Ni/a-SiO₂** samples.

	Composition (wt%)						Composition (at%)
Sample	Si	Ni	Cl	C	N	O	Atomic ratio to Si
Ni/a-SiCN	52.86	7.43	4.34	21.0	14.22	2.63	$Si_1Ni_{0.07}Cl_{0.06}C_{0.93}N_{0.54}O_{0.09}$
Ni/a-Si₃N₄	54.08	6.44	0.16	2.11	30.47	6.56	$Si_1Ni_{0.06}Cl_{0.002}C_{0.09}N_{1.13}O_{0.21}$
Ni/a-SiO₂	48.36	6.40	0.10	2.75	n.d.[a,b]	42.50[a]	$Si_1Ni_{0.06}Cl_{0.002}C_{0.13}O_{1.54}$

[a]; The amount of N and O in Ni/a-SiO_2 was measured by the EDS analysis.

[b]; Not detected (n.d.) due to the component amount being too low to be detected.

It should be noted that the similar size of Ni nanoparticles in **Ni/a-Si₃N₄** and **Ni/a-SiO₂** is favorable for discussing the effect of EMSI since the EMSI highly depends on the size of TM.

Table 1 lists the elemental compositions of the polymer-derived composites. Firstly, the annealing conditions are found to be highly effective for the nitridation and oxidation of **Ni/a-SiCN** sample to afford **Ni/a-Si₃N₄** and **Ni/a-SiO₂** samples, respectively: the nitrogen content increases by more than 50% in **Ni/a-Si₃N₄** compared with **Ni/a-SiCN** while the oxygen content in **Ni/a-SiO₂** is significantly increased. The Ni/Si atomic ratio in **Ni/a-SiCN** sample is higher than the nominal one at the precursor state (Ni/Si =0.05), indicating the release of Si-containing species such as chlorosilane species as identified by TG-MS analysis (Figure S3 (a)). Moreover, the residual chlorine could be efficiently reduced to below 0.2 wt% in both **Ni/a-Si₃N₄** and **Ni/a-SiO₂** samples. The residual chlorine elements near the metal were reported to affect the chemisorption ability of metal.[30,31] Based on the low Cl content, the effect of chlorine can be omitted in the comparison of adsorption properties between the **Ni/a-Si₃N₄** and **Ni/a-SiO₂** samples.

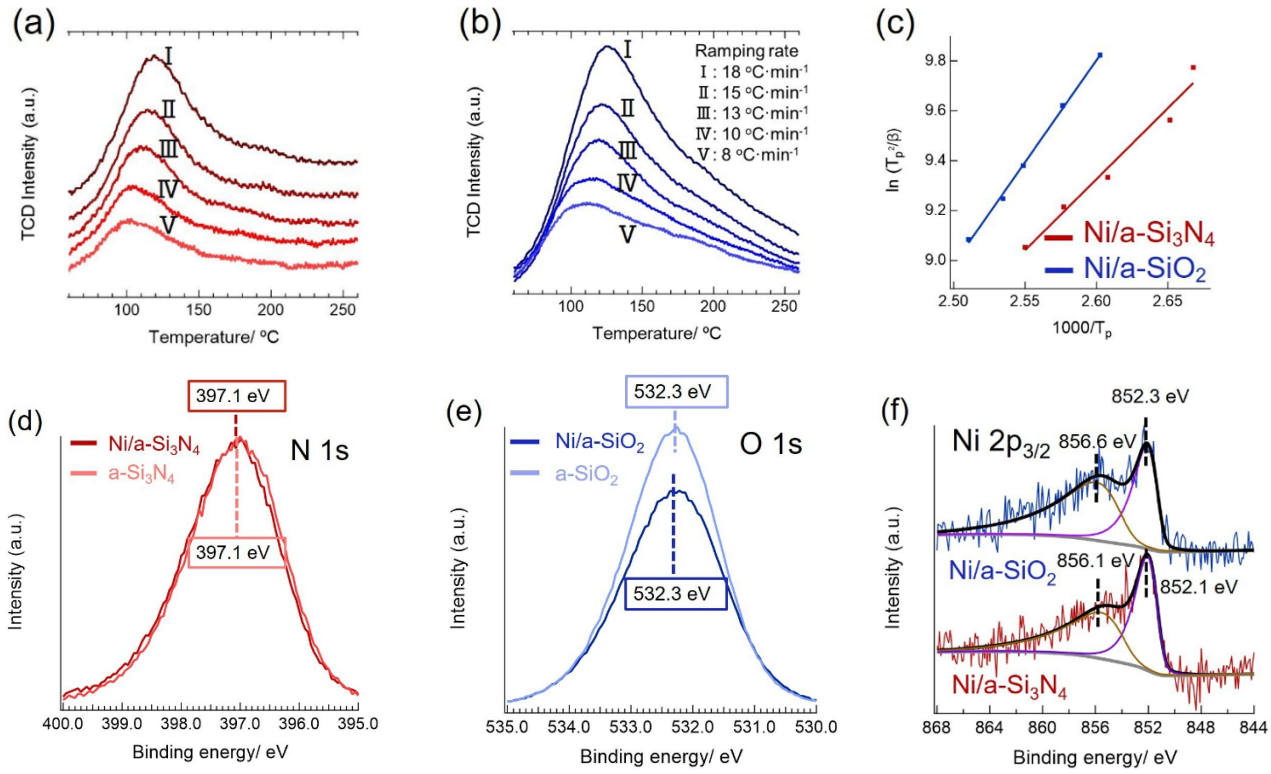

Figure 3. H_2-TPD profiles for the **Ni/a-Si_3N_4** (a), and **Ni/a-SiO_2** (b) samples after H_2 exposure at 50 °C by varying the temperature ramping rate: 18 (I), 15 (II), 13 (III), 10 (IV), and 8 (V) °C min^{-1}, respectively. (c) The plot of $ln((Tp)^2/\beta)$ against 1/Tp for **Ni/a-Si_3N_4** (dark-red line) and **Ni/a-SiO_2** (dark-blue line) samples. The activation energy for H_2-desorption of **Ni/a-Si_3N_4** and **Ni/a-SiO_2** samples were estimated from the slope of the straight line (47.4 and 68.0 kJ mol^{-1}, respectively). X-ray photoelectron spectra: (d) **Ni/a-Si_3N_4** (dark-red line) and **a-Si_3N_4** (light-red line) at N 1s core level, (e) **Ni/a-SiO_2** (dark-blue line) and **a-SiO_2** (light-blue line) samples at O 1s core level, and (f) **Ni/a-Si_3N_4** (dark-red line) and **Ni/a-SiO_2** (dark-blue line) samples at Ni $2p_{3/2}$ core levels.

The textual properties of the composites have been investigated by measuring the N_2 adsorption/desorption isotherm at –196°C. The N_2 adsorption/desorption isotherm curves for all composites in Figure 2 (h) exhibit a type I isotherm according to the IUPAC classification,[32] indicating the existence of micropores. It is generally recognized that the formation of micropores in polymer-derived ceramics is due to the release of gaseous byproducts during the early stages of the polymer-to-ceramic conversion process.[33] In addition, all the adsorption/desorption isotherm curves are composed of a hysteresis loop with a type IV[32] which suggests the formation of mesopores. As listed in Table 2, the Brunauer-Emmett-Teller (BET) surface area for the **Ni/a-Si_3N_4** sample is 308 m^2 g^{-1} which is comparable with that measured on the **Ni/a-SiO_2** sample. Moreover, the average pore diameter of these samples is almost the same, approximately 2 nm and close to that of the intermediate, **Ni/a-SiCN** sample. It should be noted that H_2 molecules can permeate through even the sub-nanometer pore channels without diffusion barriers.[34] Therefore, H_2 molecules can access the metal Ni nanoparticles embedded within the micro/mesoporous amorphous matrix without the diffusion barrier in the materials systems investigated in this study.

Table 2. BET surface area and mean pore diameter for **Ni/a-SiCN**, **Ni/a-Si_3N_4**, and **Ni/a-SiO_2** samples

Sample	S_{BET} /m^2 g^{-1}	Mean pore diameter/nm
Ni/a-SiCN	515	1.94
Ni/a-Si_3N_4	308	2.28
Ni/a-SiO_2	293	2.08

Temperature-programmed-desorption of hydrogen has been performed on the **Ni/a-Si_3N_4** and **Ni/a-SiO_2** samples to study the effect of the support matrix on the hydrogen adsorption/desorption properties on the Ni nanoparticles embedded within the amorphous matrix (Figure 3(a,b)). Regardless of the ramping rate, both samples presented a distinct peak at about 100 –130 °C, which can be assigned to the H_2 desorption from the Ni surface by considering that such a peak is not detected for the Ni-free samples; i.e. **a-Si_3N_4** and **a-SiO_2** samples, as shown in Figure S6.

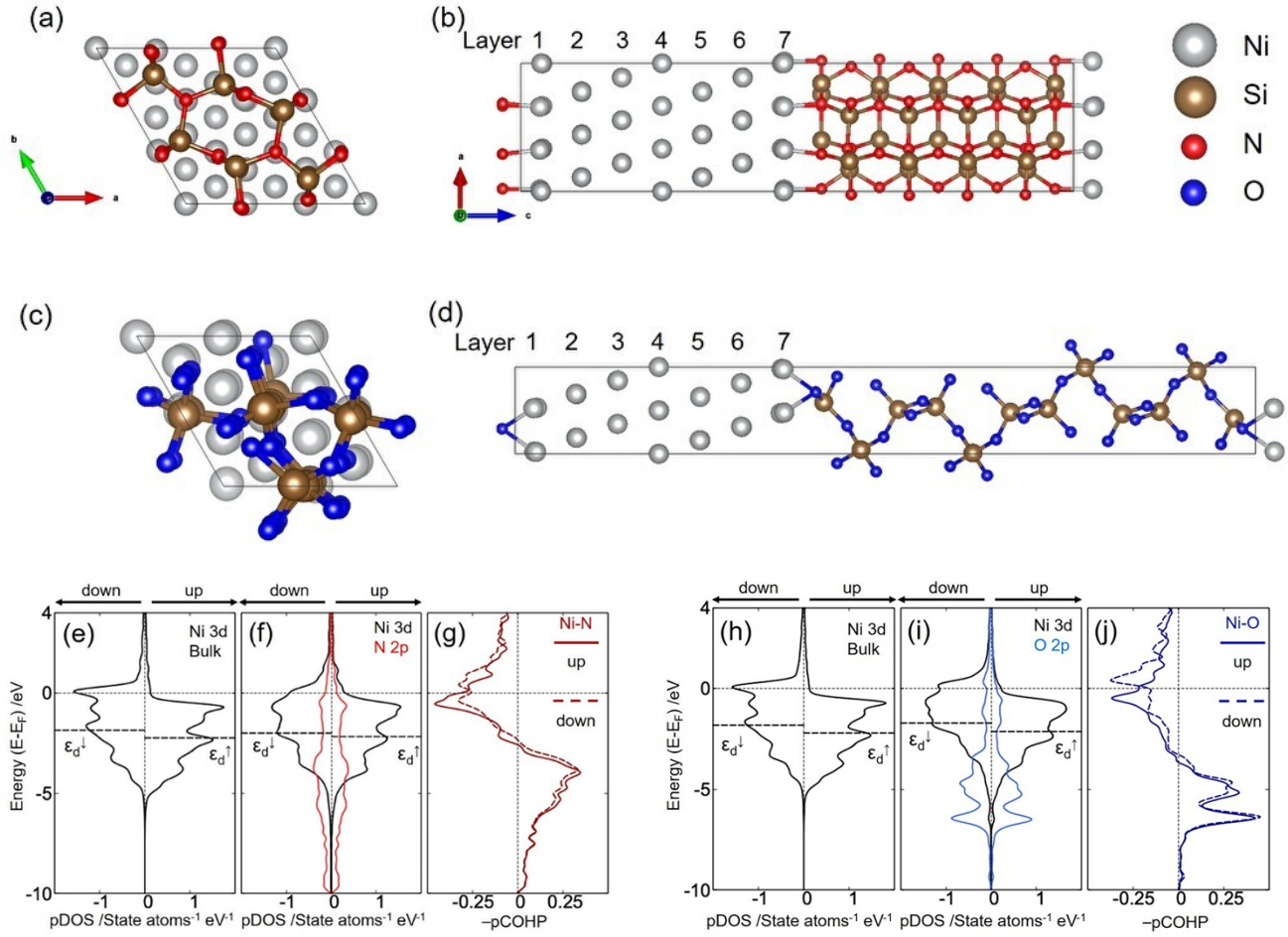

Figure 4. Interfacial models after the optimization of atomic positions: (a) Top view and (b) lateral side of Ni/β-Si_3N_4 model, (c) Top view and (d) lateral side of Ni/α-SiO_2 interfacial model. Layer 1 and 7 of Ni correspond to the interfacial region, while Layer 4 in each model corresponds to the bulk region. (e) pDOS of Ni 3d orbitals of the bulk region for the Ni/β-Si_3N_4 model. (f) pDOS of Ni 3d and N 2p orbitals of the interfacial regions for the Ni/β-Si_3N_4 model. (g) Average –pCOHP curves for Ni-N bonds at heterointerface. (h) pDOS of Ni 3d orbitals of the bulk region for the Ni/α-SiO_2 model. (i) Calculated pDOS of Ni 3d and O 2p orbitals of the interfacial regions for the Ni/α-SiO_2 model. (j) Average –pCOHP curves for Ni-O bonds at heterointerface. Fermi energy (E_F) is set at $E–E_F = 0$ eV. The d band center ε_d for spin-up (↑) and that for spin-down (↓) of Ni are depicted by a dashed line in pDOS. It should be noted that interfacial Ni is the Ni at 2.1 Å or less from the N or O atoms in two interfacial models.

The activation energy for H_2 desorption from Ni (E_{des}) has been estimated by the Redhead model.[35] By measuring the absolute temperature of a peak, T_p (K) of the H_2-TPD signal with different ramping rate, β (K min^{-1}), an Arrhenius-type plot of $\ln((T_p)^2/\beta)$ against $1/T_p$ can be obtained, and the slope corresponds to E_{des}/R (R: gas constant). As shown in Figure 3 (c), straight lines for the **Ni/a-Si_3N_4** (R^2 = 0.973) and **Ni/a-SiO_2** (R^2 = 0.998) samples are obtained, and the E_{des} values for the **Ni/a-Si_3N_4** and **Ni/a-SiO_2** have been calculated to be 47.4 and 68.0 kJ mol^{-1}, respectively. Furthermore, the desorption behaviors are well reproduced over the different batches of samples shown in Figure S7. Thus, it was concluded that the E_{des} measured for the **Ni/a-Si_3N_4** samples was about 20 to 25 kJ mol^{-1} lower than that for the **Ni/a-SiO_2** sample.

It should be noted that the measured activation energy for hydrogen desorption can exclude the diffusion barriers through the support matrix since the average pore diameters of the **a-Si_3N_4** and **a-SiO_2** support matrix are sufficiently large. In addition, the comparison of H_2-TPD profiles (Figure S6) indicates that a greater amount of hydrogen species desorbs from the nickel in the **Ni/a-SiO_2** sample. This implies that the adsorption strength between Ni and hydrogen is decreased in the **Ni/a-Si_3N_4** sample since the content and particle size of Ni in both samples are comparable, as well as the measurement condition is the same. Lee et al. reported that the higher coverage of hydrogens - the lower E_{des} of hydrogens - was observed in Ni/SiO_2 sample (E_{des} ranging from 89 kJ mol^{-1} at low coverage to 55 kJ mol^{-1} at high coverage).[36] Although the coverage of hydrogens onto Ni is low in the **Ni/a-Si_3N_4** sample as shown in Figure S6, the E_{des} is interestingly lower in the **Ni/a-Si_3N_4** sample. Therefore, the a-Si_3N_4 is experimentally expected to decrease the Ni-H adsorption strength through the electronic interaction between nickel and the a-Si_3N_4 matrix. Regarding nickel-

based catalysts, the decrease of the adsorption strength of Ni towards adsorbates finds advantageous in several catalytic reactions. For instance, in the hydrogen evolution reaction, noble metals such as ruthenium (Ru) and rhodium (Rh) exhibit superior catalytic performance compared to Ni.[37] This is partially caused by the stronger Ni-H adsorption compared to Ru-H and Rh-H. Thus, the decrease of the adsorption strength of Ni towards adsorbates potentially is favored in the catalytic application.

To investigate the electronic interaction between nickel and the amorphous matrix in more detail, the surface electronic nature of the nickel in as-synthesized **Ni/a-Si_3N_4** and **Ni/a-SiO_2** samples has been characterized by XPS analysis. The XPS peak positions of O 1s for **Ni/a-SiO_2** samples and N 1s for the **Ni/a-Si_3N_4** are not significantly different from those of the **a-SiO_2** and **a-Si_3N_4**, respectively. However, a difference is found in the regions of the Ni $2p_{3/2}$ core level as shown in Figures 3 (d,e). The **Ni/a-SiO_2** sample spectrum is composed of the two main peaks at 852.3 and 856.6 eV for the metallic Ni^0 and Ni^{2+}, respectively (Figure 3 (f)).[38] On the other hand, slight negative shifts for the two main peaks - at 852.1 and 856.1 eV, respectively - are detected for the **Ni/a-Si_3N_4** sample. Such negative shifts in XPS analysis can be interpreted as a result of the highest electron density of nickel in the **Ni/a-Si_3N_4** sample compared with that in the **Ni/a-SiO_2** sample.

The highest electron density of nickel in the **Ni/a-Si_3N_4** sample is suggested to be ascribed to the nitrogen element which displays a lower electronegativity than the oxygen element, i.e., less ability to withdraw the electron of Ni at the heterointerface between the Ni nanoparticles surface and a-Si_3N_4 matrix.

In order to further understand the effect of Ni-N and Ni-O bonding natures at heterointerface on the electronic properties of Ni, we have performed electronic structure calculations within the spin-polarized density functional theory (DFT) framework using the Ni/β-Si_3N_4 and Ni/α-SiO_2 interfacial models as shown in Figures 4(a-d) (Computational details and model construction procedure are described in supporting data). After relaxing the atomic positions, we find that the two shortest bond lengths of the Ni-N are 1.89 Å and 1.99 Å, while those of the Ni-O distance are around 1.97 Å and 2.03 Å.

As a reference, the d band center ($\varepsilon_d^{\uparrow}$ and $\varepsilon_d^{\downarrow}$) relative to the Fermi level in the bulk region (Layer 4) for the Ni (111) slab model in Figure S8 are –2.19 and –1.83 eV, while those in the surface region for the slab model are –1.98 and –1.53 eV, respectively as shown in Figure S9. It is generally observed that the d band center of surface atoms upshifts compared with that of bulk atoms.[39] This is expected because surface atoms have less coordination numbers compared with the bulk atoms, leading to increasing the electron localization, narrowing the d band, and upshifting the d band center. The projected density of states (pDOS) onto the Ni 3d orbitals of the bulk region (Layer 4) for interfacial models is shown in Figures 4 (e,h). For both models, the Ni d band center ($\varepsilon_d^{\uparrow}$ and $\varepsilon_d^{\downarrow}$) relative to the Fermi level exhibited no significant differences compared with the Ni (111) slab model. The values of $\varepsilon_d^{\uparrow}$ and $\varepsilon_d^{\downarrow}$ calculated for the Ni/β-Si_3N_4 interfacial model are found to be –2.23 and –1.86 eV, respectively. Those for the Ni/α-SiO_2 model are –2.20 and –1.84 eV, respectively. Notably, these values are consistent with the values for the bulk region for the Ni (111) slab model.

The distinctive differences in the Ni d band center are observed at the interface. As shown in Figures 4 (f,i), the Ni d band center of $\varepsilon_d^{\uparrow}$ and $\varepsilon_d^{\downarrow}$ calculated for the Ni/β-Si_3N_4 interfacial region (Layer 1 and 7) are –2.19 and –1.99 eV, respectively. Those for the Ni/α-SiO_2 interfacial region are –2.13 and –1.73 eV, respectively. Compared with the d band center of surface atoms for the Ni (111) slab model, the d band center of the Ni atoms at heterointerface in both two interfacial models is found far away from the Fermi level. This is ascribed to the interface construction which gives rise to the electron delocalization of Ni at heterointerface resulting in the downshift of the Ni d band center.

Figures 4 (f,i) also show the pDOS onto the N and O 2p orbitals at heterointerface. It is found that the interfacial O 2p orbitals are relatively localized on the lower energy region, while the interfacial N 2p orbitals are distributed from the lower energy side up to the vicinity of the Fermi level.

The projected crystal orbital Hamilton populations (pCOHP) analysis is used to visualize the hybridization natures of the Ni-N and Ni-O at the heterointerface. The bonding and antibonding populations are represented by positive and negative –pCOHP, respectively. In this study, the –pCOHP values are computed for the Ni-N and Ni-O bonds at heterointerface. From the averaged pCOHP plotting in Figures 4 (g,j), it is found that the spin-down states for both Ni-N and Ni-O hybridizations possessed lower populations for the antibonding states, compared to their spin-up states. Thus, the bonds at heterointerface for the spin-down states are more attractive than those for spin-up states. To obtain a more quantitative estimate of the bonding nature at heterointerfaces, we have calculated the average integrated –COHP (–ICOHP) up to the Fermi level over the Ni-N and Ni-O bonds at heterointerface. In general, the greater the positive –ICOHP for a bond is, the more covalent nature of the bond is.[40] The average –ICOHP values for Ni-N bonds at heterointerface are 0.69 and 0.83 for the spin-up and spin-down states, respectively, while those for Ni-O bonds at heterointerface were 0.51 and 0.71 for them. This confirms that more covalent bonds are generated between interfacial Ni and N, which is potentially driven by the lower electronegativity of the N atom relative to that of the O atom as shown in XPS analysis. It should be noted that such a strong orbital hybridization can broaden the d band and downshift the d band center of metal.[41] Therefore, we can predict from the DFT calculations that the Ni at heterointerface in the Ni/β-Si_3N_4 interface has a weaker interaction towards an adsorbate which leads to the facilitated H_2 desorption property observed for the polymer-derived **Ni/a-Si_3N_4** in this study.

Conclusions

In this work, the EMSI between Ni nanoparticles and a-Si_3N_4 matrix was deeply investigated by experimental and theoretical comparative studies. To understand and demonstrate the EMSI, we have successfully synthesized the two different nanocomposite systems, i.e., Ni nanoparticles embedded within the a-Si_3N_4 matrix and those within the a-SiO_2 matrix through the PDC route. The present

experimental and theoretical studies highlight the following results:

1. ATR-FTIR and Raman spectroscopic analyses revealed that the monomeric modifier of Ni^{2+} species as the Ni precursor had high catalytic activity towards dehydrogenation and hydrosilylation reactions to self-cross-link poly(vinylmethyl-co-methyl)silazane under our synthesis condition. Consequently, TG-MS analysis revealed that the mass loss occurring in the early step of the polymer-to-nanocomposite conversion was suppressed in **NiPSZ** sample.
2. The elemental analysis showed that both anneal conditions for the synthesis of the **Ni/a-Si_3N_4** and **Ni/a-SiO_2** samples were effective for the full nitridation and oxidation of **Ni/a-SiCN**, as well as for the complete removal of residual chlorine elements. Thus, the structural and textural properties of the **Ni/a-Si_3N_4** and **Ni/a-SiO_2** samples were comparable.
3. H_2-TPD profile analysis for the **Ni/a-Si_3N_4** and **Ni/a-SiO_2** samples indicated that the activation energy for H_2 desorption from Ni of the **Ni/a-Si_3N_4** sample (47.4 kJ mol^{-1}) was apparently lower than that of the **Ni/a-SiO_2** sample (68.0 kJ mol^{-1}). The decrease in the activation energy for the H_2 desorption of the **Ni/a-Si_3N_4** sample was governed by the downshift of the Ni d band center due to the more covalent nature of Ni-N bonds at heterointerface relative to that generated by the Ni-O bonds at heterointerface.

Combined with the experimental and theoretical results, the facilitated H_2 desorption property observed for the Ni nanoparticles embedded within the a-Si_3N_4 matrix can be ascribed to the EMSI and well explained by d band theory. The strong hybridization between the Ni and N at heterointerface exhibited the covalent natures, resulting in the further downshift of the Ni d band center at the Ni nanoparticles/a-Si_3N_4 heterointerfaces. Moreover, the embedment structure of the **Ni/a-Si_3N_4** sample contributed to enlarging the interfacial contact area, i.e., promoting the EMSI. As a result, the d band center of the embedded Ni in the **Ni/a-Si_3N_4** was decreased, which resulted in facilitated hydrogen desorption. Modulating the d band center of transition metals is a pivotal strategy for improving the catalytic performance. The catalytic activity of the **Ni/a-Si_3N_4** sample with the tuned Ni d band center has been under investigation and will be published separately

ASSOCIATED CONTENT

Supporting Information.
Experimental and computational detail, XRD patterns, Intensity ratio of ATR-FTIR absorption bands, Mass spectroscopy analysis, Ni size distribution from TEM images, H_2-TPD profiles, pDOS of Ni for a Ni slab model.

AUTHOR INFORMATION

Corresponding Author

Yuji Iwamoto — *Department of Life Science and Applied Chemistry, Graduate School of Engineering, Nagoya Institute of Technology, Nagoya, Japan;* Email: iwamoto.yuji@nitech.ac.jp

Authors

Norifumi Asakuma — *Department of Life Science and Applied Chemistry, Graduate School of Engineering, Nagoya Institute of Technology, Nagoya, Japan*
Shotaro Tada — *Department of Life Science and Applied Chemistry, Graduate School of Engineering, Nagoya Institute of Technology, Nagoya, Japan, Department of Metallurgical and Materials Engineering, Indian Institute of Technology Madras, Chennai, India*
Tomoyuki Tamura — *Department of Applied Physics, Graduate School of Engineering, Nagoya Institute of Technology, Nagoya, Japan*
Erika Kawaguchi — *Department of Life Science and Applied Chemistry, Graduate School of Engineering, Nagoya Institute of Technology, Nagoya, Japan*
Sawao Honda — *Department of Life Science and Applied Chemistry, Graduate School of Engineering, Nagoya Institute of Technology, Nagoya, Japan*
Toru Asaka — *Department of Life Science and Applied Chemistry, Graduate School of Engineering, Nagoya Institute of Technology, Nagoya, Japan*
Assil Bouzid — *IRCER, CNRS, Univ. Limoges, Limoges, France*
Samuel Bernard — *IRCER, CNRS, Univ. Limoges, Limoges, France*

Notes

The authors declare no competing financial interest.

ACKNOWLEDGMENT

This work was supported by CNRS via the International Research Project (IRP) 'Ceramics materials for societal challenges (Dr. Samuel Bernard and Prof. Y. Iwamoto), by JSPS KAKENHI, Grant Number JP20K05076, by JST SPRING, Grant Number JPMJSP2112. Norifumi Asakuma acknowledges receiving financial support from JST SPRING, Grant Number JPMJSP2112.

REFERENCES

1. Gielen, D.; Boshell, F.; Saygin, D. Climate and Energy Challenges for Materials Science. *Nat. Mater.* **2016**, *15* (2), 117–120. https://doi.org/10.1038/nmat4545.
2. Yentekakis, I. V.; Dong, F. Grand Challenges for Catalytic Remediation in Environmental and Energy Applications Toward a Cleaner and Sustainable Future. *Front. Environ. Chem.* **2020**, *1* , 1–14. https://doi.org/10.3389/fenvc.2020.00005.
3. Rodríguez-Padrón, D.; Puente-Santiago, A. R.; Balu, A. M.; Muñoz-Batista, M. J.; Luque, R. Environmental Catalysis: Present and Future. *ChemCatChem* **2019**, *11* (1), 18–38. https://doi.org/10.1002/cctc.201801248.
4. Melius, C. F. On the Role of d Electrons in Chemisorption and Catalysis on Transition Metal Surfaces. *Chem. Phys. Lett.* **1976**, *39* (2), 287–290. https://doi.org/10.1016/0009-2614(76)80076-0.
5. Zhang, L.; Zhou, M.; Wang, A.; Zhang, T. Selective Hydrogenation over Supported Metal Catalysts: From Nanoparticles to Single Atoms. *Chem. Rev.* **2020**, *120* (2), 683–733. https://doi.org/10.1021/acs.chemrev.9b00230.
6. Hammer, B.; Norskov, J. K. Why Gold Is the Noblest of All the Metals. *Nature* **1995**, *376* (6537), 238–240. https://doi.org/10.1038/376238a0.
7. Nørskov, J. K.; Abild-Pedersen, F.; Studt, F.; Bligaard, T. Density Functional Theory in Surface Chemistry and Catalysis. *Proc. Natl. Acad. Sci. U. S. A.* **2011**, *108* (3), 937–943. https://doi.org/10.1073/pnas.1006652108.
8. Baraiya, B. A.; Tanna, H.; Mankad, V.; Jha, P. K. Dressing of Cu Atom over Nickel Cluster Stimulating the Poisoning-Free CO Oxidation: An Ab Initio Study. *J. Phys. Chem. A,* **2021**, *125*

(24), 5256–5272. https://doi.org/10.1021/acs.jpca.1c02354.
9. Li, B.; Gao, W.; Jiang, Q. Electronic and Geometric Determinants of Adsorption: Fundamentals and Applications. *J. Phys. Energy* **2021**, *3* (2), 022001. https://doi.org/10.1088/2515-7655/abd295.
10. van Deelen, T. W.; Hernández Mejía, C.; de Jong, K. P. Control of Metal-Support Interactions in Heterogeneous Catalysts to Enhance Activity and Selectivity. *Nat. Catal.* **2019**, *2* (11), 955–970. https://doi.org/10.1038/s41929-019-0364-x.
11. Yan, L.; Liu, J.; Wang, X.; Ma, C.; Zhang, C.; Wang, H.; Wei, Y.; Wen, X.; Yang, Y.; Li, Y. Ru Catalysts Supported by Si_3N_4 for Fischer-Tropsch Synthesis. *Appl. Surf. Sci.* **2020**, *526* (April), 146631. https://doi.org/10.1016/j.apsusc.2020.146631.
12. Lale, A.; Mallmann, M. D.; Tada, S.; Bruma, A.; Özkar, S.; Kumar, R.; Haneda, M.; Francisco Machado, R. A.; Iwamoto, Y.; Demirci, U. B.; Bernard, S. Highly Active, Robust and Reusable Micro-/Mesoporous TiN/Si_3N_4 Nanocomposite-Based Catalysts for Clean Energy: Understanding the Key Role of TiN Nanoclusters and Amorphous Si_3N_4 Matrix in the Performance of the Catalyst System. *Appl. Catal. B Environ.* **2020**, *272*, 118975. https://doi.org/10.1016/j.apcatb.2020.118975.
13. Hullmann, D.; Wendt, G.; Ziegenbalg, G. Porous Silicon Nitride Materials as Basic Catalysts. *Chem. Eng. Technol.* **2001**, *24* (2), 147. https://doi.org/10.1002/1521-4125(200102)24:2<147::AID-CEAT147>3.0.CO;2-C.
14. Laarz, E.; Zhmud, B. V.; Bergström, L. Dissolution and Deagglomeration of Silicon Nitride in Aqueous Medium. *J. Am. Ceram. Soc.* **2004**, *83* (10), 2394–2400. https://doi.org/10.1111/j.1151-2916.2000.tb01567.x.
15. Tada, S.; Mallmann, M. D.; Takagi, H.; Iihama, J.; Asakuma, N.; Asaka, T.; Daiko, Y.; Honda, S.; Nishihora, R. K.; Machado, R. A. F.; Bernard, S.; Iwamoto, Y. Low Temperaturein Situformation of Cobalt in Silicon Nitride toward Functional Nitride Nanocomposites. *Chem. Commun.* **2021**, *57* (16), 2057–2060. https://doi.org/10.1039/d0cc07366k.
16. Asakuma, N.; Tada, S.; Kawaguchi, E.; Terashima, M.; Honda, S.; Nishihora, R. K.; Carles, P.; Bernard, S.; Iwamoto, Y. Mechanistic Investigation of the Formation of Nickel Nanocrystallites Embedded in Amorphous Silicon Nitride Nanocomposites. *Nanomaterials* **2022**, *12* (10). https://doi.org/10.3390/nano12101644.
17. Zhang, L.; Liu, X.; Wang, H.; Cao, L.; Huang, C.; Li, S.; Zhang, X.; Guan, Q.; Shao, X.; Lu, J. Size-Dependent Strong Metal-Support Interaction in Pd/ZnO Catalysts for Hydrogenation of CO_2 to Methanol. *Catal. Sci. Technol.* **2021**, *11* (13), 4398–4405. https://doi.org/10.1039/d1cy00606a.
18. Liu, L.; Corma, A. Metal Catalysts for Heterogeneous Catalysis: From Single Atoms to Nanoclusters and Nanoparticles. *Chem. Rev.* **2018**, *118* (10), 4981–5079. https://doi.org/10.1021/acs.chemrev.7b00776.
19. Panagiotopoulou, P.; Verykios, X. E. Metal-Support Interactions of Ru-Based Catalysts under Conditions of CO and CO_2 Hydrogenation. *Catalysis* **2020**, *32*, 1–23. https://doi.org/10.1039/9781788019477-00001.
20. Tada, S.; Asakuma, N.; Ando, S.; Asaka, T.; Daiko, Y.; Honda, S.; Haneda, M.; Bernard, S.; Riedel, R.; Iwamoto, Y. Novel Hydrogen Chemisorption Properties of Amorphous Ceramic Compounds Consisting of P-Block Elements: Exploring Lewis Acid-Base Al-N Pair Sites Formedin Situwithin Polymer-Derived Silicon-Aluminum-Nitrogen-Based Systems. *J. Mater. Chem. A* **2021**, *9* (5), 2959–2969. https://doi.org/10.1039/d0ta10271g.
21. Fonblanc, D.; Lopez-Ferber, D.; Wynn, M.; Lale, A.; Soleilhavoup, A.; Leriche, A.; Iwamoto, Y.; Rossignol, F.; Gervais, C.; Bernard, S. Crosslinking Chemistry of Poly(Vinylmethyl-Co-Methyl)Silazanes toward Low-Temperature Formable Preceramic Polymers as Precursors of Functional Aluminium-Modified Si-C-N Ceramics. *Dalt. Trans.* **2018**, *47* (41), 14580–14593. https://doi.org/10.1039/c8dt03076f.
22. Morais Ferreira, R. K.; Ben Miled, M.; Nishihora, R. K.; Christophe, N.; Carles, P.; Motz, G.; Bouzid, A.; Machado, R.; Masson, O.; Iwamoto, Y.; Célérier, S.; Habrioux, A.; Bernard, S. Low Temperature in Situ Immobilization of Nanoscale Fcc and Hcp Polymorphic Nickel Particles in Polymer-Derived Si-C-O-N(H) to Promote Electrocatalytic Water Oxidation in Alkaline Media. *Nanoscale Adv.* **2022**, *5* (3), 701–710. https://doi.org/10.1039/d2na00821a.
23. Mikuli, E.; Migdał-Mikuli, A.; Majda, D. Thermal Decomposition of Polycrystalline $[Ni(NH_3)_6](NO_3)_2$. *J. Therm. Anal. Calorim.* **2013**, *112* (3), 1191–1198. https://doi.org/10.1007/s10973-012-2640-8.
24. Yive, S. C. K.; Corriu, R. J. P.; Leclercq, D.; Mutin, P. H.; Vioux, A. Silicon Carbonitride from Polymeric Precursors: Thermal Cross-Linking and Pyrolysis of Oligosilazane Model Compounds. *Chem. Mater.* **1992**, *4* (1), 141–146. https://doi.org/10.1021/cm00019a029.
25. Seifollahi Bazarjani, M.; Kleebe, H. J.; Müller, M. M.; Fasel, C.; Baghaie Yazdi, M.; Gurlo, A.; Riedel, R. Nanoporous Silicon Oxycarbonitride Ceramics Derived from Polysilazanes in Situ Modified with Nickel Nanoparticles. *Chem. Mater.* **2011**, *23* (18), 4112–4123. https://doi.org/10.1021/cm200589n.
26. Balestrat, M.; Cheype, M.; Gervais, C.; Deschanels, X.; Bernard, S. Advanced Nanocomposite Materials Made of TiC Nanocrystals in Situ Immobilized in SiC Foams with Boosted Spectral Selectivity. *Mater. Adv.* **2023**, *4* (4), 1161–1170. https://doi.org/10.1039/d2ma00886f.
27. Nah, H. Y.; Kim, Y.; Kim, T.; Lee, K. Y.; Parale, V. G.; Lim, C. H.; Seo, J. Y.; Park, H. H. Comparisonal Studies of Surface Modification Reaction Using Various Silylating Agents for Silica Aerogel. *J. Sol-Gel Sci. Technol.* **2020**, *96* (2), 346–359. https://doi.org/10.1007/s10971-020-05399-5.
28. Biswas, R. K.; Khan, P.; Mukherjee, S.; Mukhopadhyay, A. K.; Ghosh, J.; Muraleedharan, K. Study of Short Range Structure of Amorphous Silica from PDF Using Ag Radiation in Laboratory XRD System, RAMAN and NEXAFS. *J. Non. Cryst. Solids* **2018**, *488* (February), 1–9. https://doi.org/10.1016/j.jnoncrysol.2018.02.037.
29. Cheng, Q.; Tian, Y.; Lyu, S.; Zhao, N.; Ma, K.; Ding, T.; Jiang, Z.; Wang, L.; Zhang, J.; Zheng, L.; Gao, F.; Dong, L.; Tsubaki, N.; Li, X. Confined Small-Sized Cobalt Catalysts Stimulate Carbon-Chain Growth Reversely by Modifying ASF Law of Fischer–Tropsch Synthesis. *Nat. Commun.* **2018**, *9* (1). https://doi.org/10.1038/s41467-018-05755-8.
30. Wan Abu Bakar, W. A.; Ali, R.; Mohammad, N. S. The Effect of Noble Metals on Catalytic Methanation Reaction over Supported Mn/Ni Oxide Based Catalysts. *Arab. J. Chem.* **2015**, *8* (5), 632–643. https://doi.org/10.1016/j.arabjc.2013.06.009.
31. Li, M.; Bi, F.; Xu, Y.; Hao, P.; Xiang, K.; Zhang, Y.; Chen, S.; Guo, J.; Guo, X.; Ding, W. Effect of Residual Chlorine on the Catalytic Performance of Co_3O_4 for CO Oxidation. *ACS Catal.* **2019**, *9* (12), 11676–11684. https://doi.org/10.1021/acscatal.9b03797.
32. Sing, K. S. W. Reporting Physisorption Data for Gas/Solid Systems with Special Reference to the Determination of Surface Area and Porosity (Recommendations 1984). *Pure Appl. Chem.* **1985**, *57* (4), 603–619. https://doi.org/10.1351/pac198557040603.
33. Schitco, C.; Bazarjani, M. S.; Riedel, R.; Gurlo, A. NH3-Assisted Synthesis of Microporous Silicon Oxycarbonitride Ceramics from Preceramic Polymers: A Combined N_2 and CO_2 Adsorption and Small Angle X-Ray Scattering Study. *J. Mater. Chem. A* **2015**, *3* (2), 805–818. https://doi.org/10.1039/c4ta04233f.
34. Wang, S.; Zhao, Z. J.; Chang, X.; Zhao, J.; Tian, H.; Yang, C.; Li, M.; Fu, Q.; Mu, R.; Gong, J. Activation and Spillover of

Hydrogen on Sub-1 Nm Palladium Nanoclusters Confined within Sodalite Zeolite for the Semi-Hydrogenation of Alkynes. *Angew. Chemie - Int. Ed.* **2019**, *58* (23), 7668–7672. https://doi.org/10.1002/anie.201903827.

35. Redhead, P. A. Thermal Desorption of Gases. *Vacuum* **1962**, *12* (4), 203–211. https://doi.org/10.1016/0042-207X(62)90978-8.
36. LEE, P. Adsorption-Desorption Kinetics of H2 from Supported Nickel Catalysts. *J. Catal.* **1982**, *73* (2), 272–287. https://doi.org/10.1016/0021-9517(82)90100-2.
37. Nørskov, J. K.; Bligaard, T.; Logadottir, A.; Kitchin, J. R.; Chen, J. G.; Pandelov, S.; Stimming, U. Trends in the Exchange Current for Hydrogen Evolution. *J. Electrochem. Soc.* **2005**, *152* (3), J23. https://doi.org/10.1149/1.1856988.
38. Fadaeerayeni, S.; Shan, J.; Sarnello, E.; Xu, H.; Wang, H.; Cheng, J.; Li, T.; Toghiani, H.; Xiang, Y. Nickel/Gallium Modified HZSM-5 for Ethane Aromatization: Influence of Metal Function on Reactivity and Stability. *Appl. Catal. A Gen.* **2020**, *601* (April). https://doi.org/10.1016/j.apcata.2020.117629.
39. Vojvodic, A.; Nørskov, J. K.; Abild-Pedersen, F. Electronic Structure Effects in Transition Metal Surface Chemistry. *Top. Catal.* **2014**, *57* (1–4), 25–32. https://doi.org/10.1007/s11244-013-0159-2.
40. Liu, Y.; Wang, R.; Wang, Z.; Li, D.; Cui, T. Formation of Twelve-Fold Iodine Coordination at High Pressure. *Nat. Commun.* **2022**, *13* (1), 4–10. https://doi.org/10.1038/s41467-022-28083-4.
41. Zhao, X.; Li, X.; An, L.; Iputera, K.; Zhu, J.; Gao, P.; Liu, R. S.; Peng, Z.; Yang, J.; Wang, D. Nitrogen-Inserted Nickel Nanosheets with Controlled Orbital Hybridization and Strain Fields for Boosted Hydrogen Oxidation in Alkaline Electrolytes†. *Energy Environ. Sci.* **2022**, *15* (3), 1234–1242. https://doi.org/10.1039/d1ee03482k.

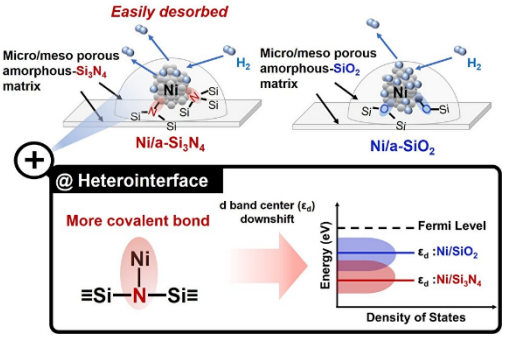
Easily desorbed
Micro/meso porous amorphous-Si3N4 matrix
H2
Ni
Si
N
Ni/a-Si3N4
Micro/meso porous amorphous-SiO2 matrix
O
Ni/a-SiO2
@ Heterointerface
More covalent bond
≡Si—N—Si≡
d band center (εd) downshift
Fermi Level
εd :Ni/SiO2
εd :Ni/Si3N4
Energy (eV)
Density of States